

Spin waves and local magnetizations on the Penrose tiling

Attila Szallas and Anuradha Jagannathan

Laboratoire de Physique des Solides, CNRS-UMR 8502, Université Paris-Sud, 91405 Orsay, France

(Dated: October 24, 2018)

We consider a Heisenberg antiferromagnet on the Penrose tiling, a quasiperiodic system having an inhomogeneous Neel-ordered ground state. Spin wave energies and wavefunctions are studied in the linear spin wave approximation. A linear dispersion law is found at low energies, as in other bipartite antiferromagnets, with an effective spin wave velocity lower than in the square lattice. Spatial properties of eigenmodes are characterized in several different ways. At low energies, eigenstates are relatively extended, and show multifractal scaling. At higher energies, states are more localized, and, depending on the energy, confined to sites of a specified coordination number. The ground state energy of this antiferromagnet, and local staggered magnetizations are calculated. Perpendicular space projections are presented in order to show the underlying simplicity of this “complex” ground state. A simple analytical model, the two-tier Heisenberg star, is presented to explain the staggered magnetization distribution in this antiferromagnetic system.

PACS numbers: 71.23.Ft, 75.10.Jm, 75.10.-b

I. INTRODUCTION

Theoretical investigations of the Heisenberg model involving localized spins on a quasiperiodic structure are motivated by experiments performed on a class of magnetic quasicrystals, the icosahedral ZnMgR (R: rare-earth) alloys¹. Short range antiferromagnetic correlations and anomalous slow dynamics have been observed at temperatures below 4K in ZnMgHo, and below 5.8 K in ZnMgTb². These experiments raise the question of what types of magnetic ordering can exist in systems with quasiperiodic structural order. Several theoretical studies of both classical^{3,4} and quantum^{5,6,7,8} models of interacting local moments in two dimensional quasiperiodic geometries have been carried out. These calculations show ground states characterized by a complex inhomogeneous magnetic order. This quasiperiodic ground state, and magnon modes are investigated in detail in the present paper.

We consider spins located on vertices of the Penrose tiling, which was introduced⁹ as an example of a deterministic nonperiodic structure and later found to be relevant for quasicrystals¹⁰. The Penrose tiling is the planar version of the three dimensional icosahedral tiling used in the description of a large number of quasicrystalline alloys. At $T=0$, since there is no frustration in the model, one expects a Néel ordered ground state, with equal and oppositely directed sublattice magnetizations. We will consider the case of $S = \frac{1}{2}$, the case of greatest theoretical interest, as quantum effects are expected to be strongest. An interesting related problem concerns the entanglement properties of spins in such hierarchical environments, a question that is currently receiving attention in view of the applications to quantum computing.

This paper follows an earlier Brief Report¹¹, where some early results were presented. In this paper we describe the method used in some detail, and we present a more complete description of the ground state properties, spin wave spectrum, magnon velocity, and eigenmodes.

The numerical calculations are done within the linearized spin wave (LSW) approximation, using periodic approximants of the Penrose tiling. We show as well that the magnetization results can be qualitatively explained in terms of a simple analytic model of tree clusters.

In Sec.II we provide some background on the Heisenberg antiferromagnet as well as the Penrose tiling for those not familiar with this quasiperiodic structure. Sec.III presents the method used, and describes the finite samples that we studied numerically. Sec.IV presents results for the magnon spectrum and density of states. In Sec.V we give the results for the ground state energy, and discuss the inhomogeneous local staggered magnetizations. Sec.VI presents a simple analytical model to explain the numerical results. Sec.VII resumes the main conclusions.

II. HEISENBERG HAMILTONIAN AND THE PENROSE TILING

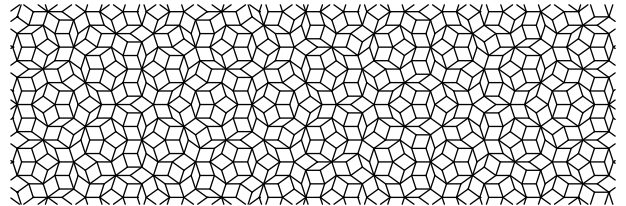


FIG. 1: A finite patch of the perfect Penrose tiling.

A. The Heisenberg Hamiltonian.

We consider the nearest-neighbor antiferromagnetic spin- $\frac{1}{2}$ Heisenberg model,

$$H = J \sum_{\langle i,j \rangle} \mathbf{S}_i \cdot \mathbf{S}_j, \quad J > 0, \quad (1)$$

where $\langle i, j \rangle$ are pairs of linked vertices of the Penrose tiling. The antiferromagnetic coupling J is taken to be the same for all bonds. The tiling is bipartite, in that sites belong to one of two sublattices A and B, and the J -terms couple a spin on sublattice A to spins lying on sublattice B and vice-versa. This property ensures that there is no frustration, i.e., if one considers classical spin variables, the ground state is one for which all bonds are “satisfied” – with all the A-sublattice spins pointing in one direction and B-sublattice spins pointing in the opposite direction. This is our reference state with long range staggered magnetic order for our calculations at $T = 0$ using the spin wave approximation. At finite temperature, the long range order will be destroyed due to the Mermin-Wagner-Hohenberg theorem¹⁷, although short range correlations will persist. We now recall some properties of the ground state of some unfrustrated Heisenberg antiferromagnets, shown in earlier studies.

1. Role of the dimension and the spin

When the spins are quantum variables, the energy of the ground state is lower than the classical value, due to quantum fluctuations or “spin waves” in the case of periodic structures. As studies using a variety of analytical and numerical methods have shown (see review¹²), the effects of quantum fluctuations vary depending on the dimension, on the spin quantum number S , and the type of structure. Quantum fluctuations are expected to become smaller as S increases, and as the dimension increases. It can be shown that, for hypercubic lattices, the spin wave expansion in fact is an expansion in $1/zS$, where $z = 2d$. For $d = 2$ and $S = \frac{1}{2}$, as in the square lattice or the honeycomb lattice, it was an open question for some time whether quantum fluctuations would be strong enough to destroy long range order, until enough evidence¹³ was presented in favor of long range order.

2. Role of the coordination number

In a given dimension, and for simple lattices, one can ask what the local quantum fluctuations are when the coordination number is changed. In two dimensions, two examples of unfrustrated systems are the square lattice with $z = 4$ and the honeycomb lattice with $z = 3$ (see the review in¹⁴). Spin wave calculations, as well as Quantum Monte Carlo calculations^{13,15} have shown that the order parameter is smaller in the $z = 3$ case. The values of the

staggered magnetization, defined by the value of $m_s = |\langle S_i^z \rangle|$ as obtained by QMC calculations are $m_s^{sq} = 0.3173$ and $m_s^{hc} = 0.2788$ (with sq and hc standing for square lattice and honeycomb lattice respectively). This is in accord with the already remarked tendency towards a less classical behavior for systems of lower dimension, hence fewer nearest neighbors.

In contrast, as pointed out in¹⁶, when the coordination number is not constant, the local magnetization tends to be in fact larger when z is smaller. In the dice lattice, where sites can have $z = 3$ and $z = 6$, spin wave theory and QMC calculations have shown that it is the small z sites that have the larger value of the local staggered magnetization, with $m_s^{z=6} = 0.3754$ while $m_s^{z=3} = 0.4381$. This result shows the “counter-intuitive” trend towards a *less* classical behavior for sites of bigger z in structures having a distribution of z values. Other systems showing this tendency include the quasiperiodic octagonal tiling and, as shown in¹¹, the Penrose tiling.

B. The Penrose tiling.

We now describe the Penrose tiling, along with some of its properties. As shown in Fig.1, which shows a finite portion of a perfect tiling, the tiles of this structure are a pair of rhombuses of angles $\pi/5$ (thin rhombus) and $2\pi/5$ (thick rhombus). The edge length will be taken to be $a = 1$.

1. Symmetries

One remarkable feature is that despite the absence of perfect translational invariance, patterns of arbitrarily large size in different regions of the tiling can be made to overlap (“local isomorphism”). The mean repetition distance of a pattern of linear size R is proportional to R , a property that replaces the strict translational invariance of crystalline structures. Rotational invariance holds in the same “weak” sense – for any given pattern, its equivalent under rotation by a multiple of $2\pi/5$ can be found elsewhere on the tiling.

The Penrose tiling possesses a hierarchical symmetry, being invariant under so-called inflation and deflation transformations. Inflation is a reversible operation which can be thought of as a set of decimations of vertices of the tiling, followed by a re-connection of the new vertices. The new tiling is defined on a length scale that is bigger by the factor $\tau = \frac{\sqrt{5}+1}{2}$ (the golden mean). The equivalence of the old and new tilings means here that no environments are created or destroyed in the process of inflation or deflation, and that one can find an exact match between any arbitrary (finite) regions of the two tilings.

A rhombus-based structure such as the one shown in Fig.1 is a two-sublattice system. On the infinite tiling,

the two sublattices are equivalent, as regards the frequencies of the different vertices (see subsection below).

2. Local environments

As Fig.2 shows, many kinds of vertices are present in the tiling. In this paper, we have chosen to classify properties of vertices according to their coordination number z . These site coordination numbers range from 3 to 7 in the Penrose tiling, with the average value \bar{z} being exactly 4. The figure shows the seven local environments possible for coordination numbers $z = 7, 6, 5, 4$ and 3. The first figure shows a five-fold symmetric site, which in fact comes in two varieties, the F (for football cluster) and the S (for star cluster). The properties of these sites under decimation are different. More will be said on these sites when we discuss the results for the ground state staggered magnetization distribution. We note that in the infinite tiling, each of the sublattices A and B have the same distribution of vertices of each type.

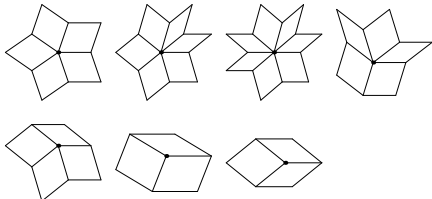


FIG. 2: Local environments in the Penrose tiling.

3. The Penrose tiling viewed as a five dimensional object

One standard method¹⁸ to obtain the Penrose tiling is by projecting a subset of vertices of a five dimensional cubic lattice onto a plane of a certain irrational orientation that is determined by the requirement of five-fold symmetry. As described in the Appendix, vertices are projected only if they lie within a five-dimensional cylinder that runs parallel to the “physical” xy plane. This approach to generating the quasiperiodic tiling allows one an alternative visualization of the Penrose tiling in “perpendicular space” - i.e. the vertices are projected onto the orthogonal three dimensional subspace.

When the Penrose tiling is thus mapped into perpendicular space, one sees (as illustrated in the Appendix in Fig.20), that the vertices now lie within four flat pentagon-shaped regions. Each family of sites of Fig.2 projects into a *distinct* domain – in other words, the perpendicular space representation allows us to separate sites according to their coordination number. We will use this useful property of the Penrose tiling in order to represent the complex antiferromagnetic ground state in a simpler way in Sec.V.

III. THE LINEAR SPIN-WAVE APPROXIMATION

This unfrustrated Heisenberg antiferromagnet is expected to have long range order at zero temperature, as remarked earlier. In the ground state, spins acquire a non-zero magnetization along the z -direction, with the total staggered magnetization of $N = \sum_i \langle \epsilon_i S_i^z \rangle \neq 0$ where $\epsilon_i = \pm 1$ depends on whether the site is on the A or B sublattice.

Assuming that quantum fluctuations are small, one can expand around the classical antiferromagnetic ground state in which $\langle \epsilon_i S_i^z \rangle = S$ for all sites. We introduce, according to standard definitions (see for example¹²), Holstein-Primakoff boson operators for the sites on the two sublattices: a_i, a_i^\dagger for sites on the A sublattice, b_i, b_i^\dagger for sites on the B sublattice. The boson operators account for deviations from the classical configuration, with the spin deviation operator on A-sublattice sites given by $a_i^\dagger a_i = \hat{n}_i \equiv S - \hat{S}_i^z$ and on B sublattice sites $b_j^\dagger b_j = \hat{n}_j \equiv S + \hat{S}_j^z$. After linearization, the Hamiltonian is

$$H_{LSW} = -JS(S+1)N_b + JS \sum_{\langle ij \rangle} (a_i^\dagger a_i + b_j^\dagger b_j + a_i^\dagger b_j^\dagger + b_j a_i)$$

where $N_b = 2N$ is the number of bonds, N is the number of sites. This quadratic Hamiltonian can be diagonalized by a generalized Bogoliubov transformation, as shown by White, Sparks and Ortenburger¹⁹. Note that the diagonalization can be carried out in the real space basis, and that there is no need to introduce collective operators as in periodic systems.

A. Outline of numerical calculation scheme.

In the expressions that follow, we number the sites such that the sites on sublattice A come first ($i = 1, \dots, N/2$), followed by the sites on sublattice B ($i = N/2 + 1, \dots, N$). The quadratic term in H_{LSW} can then be written in compact form in terms of the vector $X^T = (a_1, a_2, \dots, a_{N/2}, b_1^\dagger, \dots, b_{N/2}^\dagger)$ as

$$H_{LSW} = JSX^\dagger H_2 X \quad (2)$$

where H_2 is a real symmetric matrix of four $\frac{N}{2} \times \frac{N}{2}$ blocks:

$$H_2 = \begin{pmatrix} Z_A & C \\ C^T & Z_B \end{pmatrix} \quad (3)$$

Z_A and Z_B are diagonal matrices, with $(Z_A)_{ii} = z_i$, the coordination numbers on sublattice A, with a similar definition on sublattice B. The connectivities of the sites are given in the off-diagonal blocks, C: $C_{ij} = 1$ if i and j are nearest neighbors and $C_{ij} = 0$ otherwise. Details of the numerical diagonalization using this real space basis are described in⁶, where the LSW solution for the

ground state of the octagonal tiling was obtained. The main steps of the calculation will be outlined here for completeness.

One seeks the canonical transformation taking the set $\{a_i, b_j\}$ to a set of boson operators $\{\alpha_m, \beta_m\}$, in which the Hamiltonian is diagonal:

$$H_{LSW} = E_0 + \sum_{m=1}^{N/2} \Omega_m^+ \alpha_m^\dagger \alpha_m + \Omega_m^- \beta_m^\dagger \beta_m \quad (4)$$

where E_0 is the ground state energy

$$E_0 = -JS(S+1)N_b + JS \sum_{m=1}^{N/2} \Omega_m^- \quad (5)$$

Two of the eigenmodes, $a_{N/2}$ and $b_{N/2}$, correspond to zero eigenmodes, and arise due to a global rotation of all the spins. These should be excluded from the diagonalization procedure, which transforms the remaining $(N-2)$ operators. The generalized Bogoliubov transformation from the set $\{a, b\}$ to the set $\{\alpha, \beta\}$ is $X_m = T_{mi} X'_i$ where $X'^T = (\alpha_1, \dots, \alpha_{N/2-1}, \beta_1^\dagger, \dots, \beta_{N/2-1}^\dagger)$. The rectangular T-matrix has the following structure:

$$T = \begin{pmatrix} A_{1,1} & \dots & \dots & A_{1,N} \\ \dots & \dots & \dots & \dots \\ \dots & \dots & \dots & \dots \\ A_{\frac{N}{2}-1,1} & \dots & \dots & A_{\frac{N}{2}-1,N} \\ B_{1,1} & \dots & \dots & B_{1,N} \\ \dots & \dots & \dots & \dots \\ \dots & \dots & \dots & \dots \\ B_{\frac{N}{2}-1,1} & \dots & \dots & B_{\frac{N}{2}-1,N} \end{pmatrix} \quad (6)$$

The transpose of the row vectors of this matrix, denoted by A_m and B_m , correspond to solutions of the eigenvalue equation

$$\begin{aligned} gH_2 A_m &= \Omega_m^+ A_m \\ gH_2 B_m &= -\Omega_m^- B_m \end{aligned} \quad (7)$$

where the first equation holds for matrix elements of the rows in the upper half of T (the ‘‘positive subspace’’), and the second for the rows in the lower half of T (the ‘‘negative subspace’’). g is the matrix of commutators $g_{ij} = [X_i, X_j^\dagger]$,

$$g_{ij} = \pm \delta_{ij} \quad (8)$$

where the sign depends on whether i corresponds to the positive or the negative subspace. The new operators X' obey the same type of commutation relations $[X'_i, X'^\dagger_j] = g'_{ij} = \pm \delta_{ij}$ (where $i, j = 1, \dots, N/2 - 1$).

The T-matrix should satisfy

$$T^\dagger g T = g' \quad (9)$$

We note that in degenerate subspaces, a generalization of the Gram-Schmidt orthogonalization must be carried out with respect to the matrix g , in order to satisfy Eq.9.

B. Finite size samples for numerical calculations.

Our numerical solution of the linearized spin wave Hamiltonian is carried out on finite samples, using LAPACK²⁰. We have mentioned in the previous section that quasiperiodic tilings can be considered as projections of a simpler higher dimensional periodic systems. For our calculations, we have considered two types of samples. The first type are finite samples obtained by projection from 5D, for which we assumed open boundary condition. Such samples have the usual problem of spurious boundary modes. When considering averages over the entire spectrum, however, as one does in the computation of the order parameter, we found good agreement between these finite samples, and periodic approximants described below. More precisely, spins deep in the interior of these samples behave in the same way as the spins in the boundary-free periodic approximants, described next.

In order to apply periodic boundary conditions, we have considered the so-called Taylor approximants of the Penrose tiling¹⁸. These rectangular samples are obtained by slightly tilting the projection (or applying a ‘‘shear’’), so that the resulting projection has a finite periodic length in the x- and y-directions, as shown in Fig.21. These approximants clearly break the hierarchical and five-fold rotational symmetry of the Penrose tiling at length scales comparable to the repetition length. However, one can generate Taylor approximants of bigger and bigger size, and thus approach the infinite Penrose tiling. Our samples have the additional property of having an equal number of sites in the A and B sublattices, thus ensuring a total spin of zero in the ground state. We considered approximants of 94, 246, 644, 1686, 4414 and 11556 sites.

IV. MAGNON SPECTRUM AND WAVEFUNCTIONS

A. Energy spectrum and density of states. Linear dispersion law.

The numerical Bogoliubov transformation gives the energies Ω_m^\pm as well as the T-matrix for each of the systems considered. The two sets of energies Ω_m^+ and Ω_m^- become identical in the limit of infinite size when sublattices A and B become strictly equivalent. In our case, since the two sublattices are not identical, the numerical values are slightly different (less than a percent for the larger systems and not visible on the scale of our figures).

Fig.3a) shows the integrated density of states (IDOS). We used the following expression for the IDOS,

$$N(E) = \frac{2}{N} \sum_{m=1}^{N/2} \theta(E - \Omega_m^+) \quad (10)$$

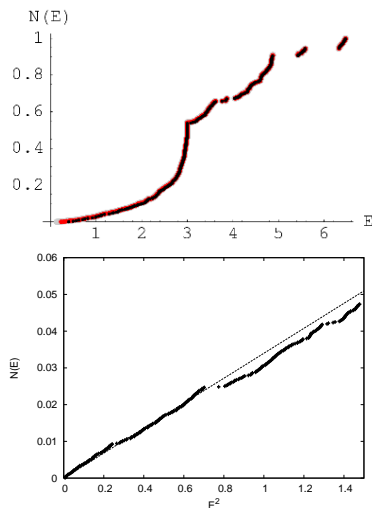


FIG. 3: a)(Color online) Integrated density of states $N(E)$ versus E (expressed in units of J) calculated for three consecutive approximants (black dots : $N = 644$, red dots : $N = 1686$, grey : $N = 4414$). b) Low energy tail of $N(E)$ versus E^2 (the straight line is a fit to the data).

The energy E is expressed in units of J , and the factor 2 arises because the sum includes only half of the complete spectrum. Data for for three successive Taylor approximants has been plotted, with the points in light gray correspond to the largest system size, points in red to the medium size, and points in black to the smallest size. The integrated DOS is only slightly size dependent, as seen by the overlapping of the three sets of data points. The salient features of the figure are the several groups of closely spaced energy levels, the main gaps, which are stable with increasing system size, and a discrete jump at the energy $E = 3$, corresponding to a macroscopic degeneracy, as discussed below.

The locations of gaps are more easily seen in the graph of the smoothed derivative of $N(E)$ – the density of states (DOS), which is shown in Fig.4. One sees the characteristic fluctuating form of the density of states typical of quasiperiodic systems.

One can distinguish several groups of energies separated by gaps. The highest energy bands around the values $E \approx 5.4$ and $E \approx 6.4$, correspond to wavefunctions that are localized on the 6- and 7-fold sites, as will be shown shortly. Lying below these in energy are the states centered primarily on the 5-fold sites. The peak at the exact value of $E = 3$ corresponds to string-like states living on the $z = 3$ sites. The lowest energies correspond to states of relatively extended character, as we will discuss below.

As shown in Fig.3b) the low energy part of the IDOS can be fitted to a power law of the energy, $N(E) \sim E^2$ reflecting a linear dispersion of the magnon modes in this region of the spectrum. Fitting to a form $N(E) = E^2/(8\pi c^2)$ gives a sound velocity on the Penrose tiling

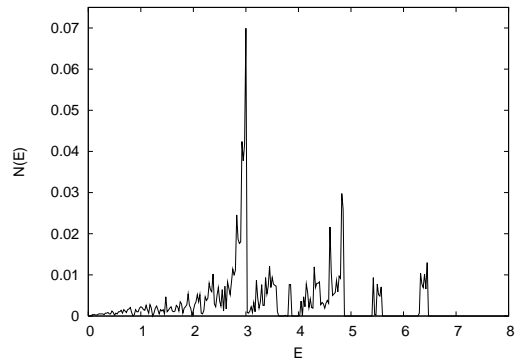


FIG. 4: Density of states calculated for the Taylor 6 approximant ($N=11556$ sites).

of $c = 1.08J$. It is interesting to compare this result for c with the corresponding values on the square lattice and the octagonal tiling, both having in common with the Penrose tiling the same value of the classical energy per spin $E_{cl}/N = -2JS^2$. This value is $c_{sq} = 2\sqrt{2}JSa \approx 1.41J$ on the square lattice (for edge length $a = 1$ and $S = 1/2$). On the octagonal tiling, our estimated value is $c_{octa} \approx 1.3J$, in agreement with Milat and Wessel's IDOS data⁶. To resume, an acoustic-type dispersion relation is obeyed at long wavelengths, with a spin wave velocity which is smaller than in the octagonal tiling, which is in turn smaller than the value on the square lattice. This is presumably due to the fact that the density of sites is largest in the Penrose systems, followed by the octagonal tiling, and finally the square lattice.

B. Wavefunctions.

We now discuss the magnon wavefunctions and their spatial characteristics for the different parts of the energy spectrum. We first show that the coordination number plays an important role in determining the extent to which a site participates in the wavefunction for a given eigenmode, $\psi^{(E)}$. This can be seen from Figs.5a) through e), which show the weight fractions as a function of the energy, for each of the five values of the coordination number z . The weight fractions were defined as

$$f_n = \sum_{i \in F_n} |\psi_i^{(E)}|^2 / \sum_j |\psi_j^{(E)}|^2 \quad (11)$$

where the F_3, F_4, \dots are the subsets of sites whose coordination numbers are $z = 3, 4, \dots$. Only sites of sublattice A are considered (a similar calculation for sublattice B gives the same results).

The plots of the weight fractions show a number of interesting properties of the magnon modes. In particular, they show the preponderance of certain types of site in the different energy bands. Thus it is clear from Fig.5 e) that the highest energies correspond to states having

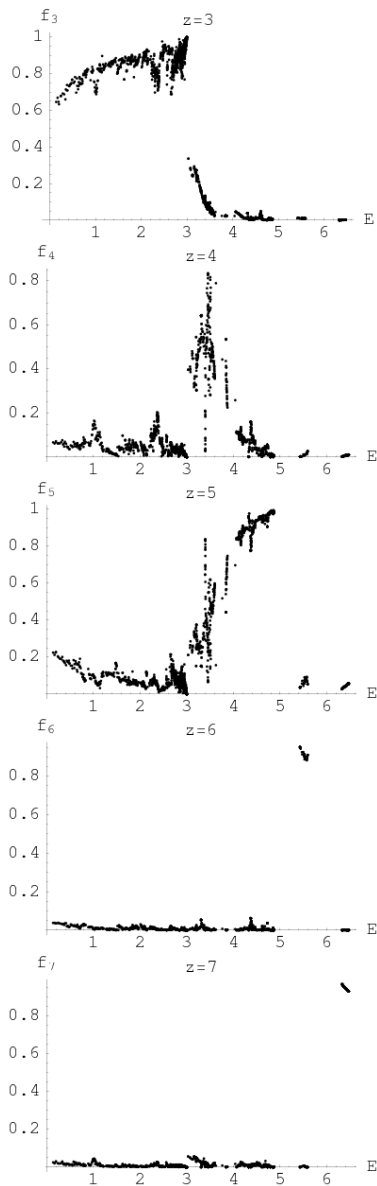


FIG. 5: a) - e) Weight fractions f_n (see text) as a function of E for $z = n$ ($n = 3, \dots, 7$), as computed for the Taylor 5 approximant ($N=4414$ sites).

a large amplitude on sites of $z = 7$. The highest energy band has a width of about 0.16 and is centred around $E = 6.4$. Fig.7a) represents one such state in real space, with sites are shown with varying intensity depending on the square of the wavefunction amplitude. The darkest spots are those on sites with $z = 7$.

The group of states next highest in energy are those involving $z = 6$ sites, and correspond to energies in the range $5.43 < E < 5.49$. These states have a smaller dispersion than the states in the topmost group of energies, reflecting the fact that the six-fold sites are significantly fewer in number than the seven-fold sites.

The middle band of energies, $3 < E < 5$ arises for

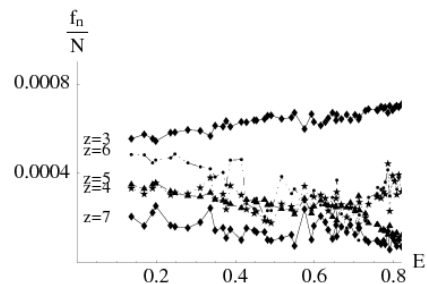


FIG. 6: The average value of $\psi_i(E)^2$ per site for each z plotted against E for states in the bottom of the spectrum.

states involving sites of $z = 5$, which account for about 30% of the sites. From Fig.5c) one sees that the four-fold sites are particularly important in a narrow range of energy within this band.

As seen by the large step in $N(E)$ at $E = 3$, a large number of degenerate states occur at this energy. This is due to wavefunctions that have their entire support on the $z = 3$ sites. These are string-like states forming closed loops – on length scales that range from a small ring (around the footballs, for example) to being as large as the system size. A linear combination of such degenerate states is shown in Fig.7b).

The lowest energy states, for $E \leq 1$, are the closest to extended states. The wavefunction amplitudes depend less sensitively on the site coordination number. The fact that all sites participate is best seen from Fig.6, where we have plotted for each of the five z -values the average probability for a given site, f_n/N_n , (where N_n is the number of sites of the n th family), as a function of the energy E . Clearly, for the low energy states, the probability amplitude is nonzero for all the values of z . On the other hand, not all of the sites participate in a given wavefunction, and for a given energy the wavefunction is mainly confined to a set of disconnected patches. The lower the energy, the larger the patches where the wavefunction is non-zero. Figs.7c) and d) show the states corresponding to two energies. For $E = 0.8887$ there are many closely spaced small patches. As the energy gets smaller, the patches of non-zero amplitude get larger, along with the spacing between them, and at energy $E = 0.1692$, for example, the wave function has two large patches (which are of course repeated periodically, due to the boundary conditions).

To resume, the dimension of the support of eigenstates decreases as a function of the energy, from two at small E , to one at $E = 3$, tending to zero at the highest energies.

C. Perpendicular space representation of the wavefunctions

In the preceding section we alluded to the fact that the perpendicular space representation of the Penrose tiling

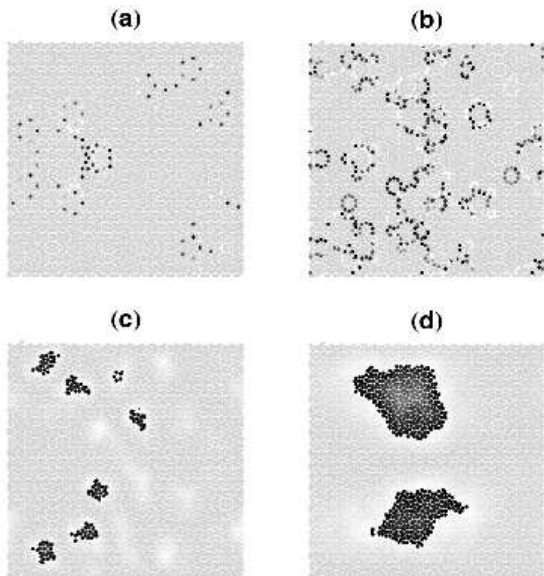


FIG. 7: Intensity plots representing the probability $\psi_i(E)^2$ for different energies E (a darker shade corresponds to a higher probability): a) $E = 6.469$ b) $E = 3.0000$ c) $E = 0.8887$ d) $E = 0.1692$. The solutions have been obtained for the Taylor 5 approximant ($N=4414$ sites).

is a useful way to see the environment-dependence of spatially varying quantities. We now illustrate this in the case of the four wavefunctions shown in Figs.7 represented in perpendicular space by Figs.8. Each vertex of the Taylor approximant is mapped (see the Appendix for more details) onto a point $\{x_\perp, y_\perp, z_\perp\}$. We show the projection in the plane $z_\perp = 2$ of the Penrose tiling, with regions shaded according to the local value of the wavefunction. Specifically, the intensity of the spot at site i is proportional to the value of $|\psi_i(E)|^2$. Fig.8a) shows the perpendicular space projection for the wavefunction corresponding to the energy $E = 6.469$. The spots of maximum intensity are in the region that corresponds to $z = 7$ (as seen in Fig.20). Fig.8b) shows, similarly, that the wavefunction for $E = 3$ is non-zero for the region corresponding to $z = 3$. The last two figures show wavefunctions that are delocalized in perpendicular space (ie, all sites are involved, regardless of the value of the coordination number).

D. Participation ratio and multifractal analysis.

We present the results for the inverse participation ratio (IPR), defined by

$$P^{-1}(E) = \frac{\sum_j |\psi_j(E)|^4}{(\sum_j |\psi_j(E)|^2)^2}$$

Recall that as N is increased, the inverse participation

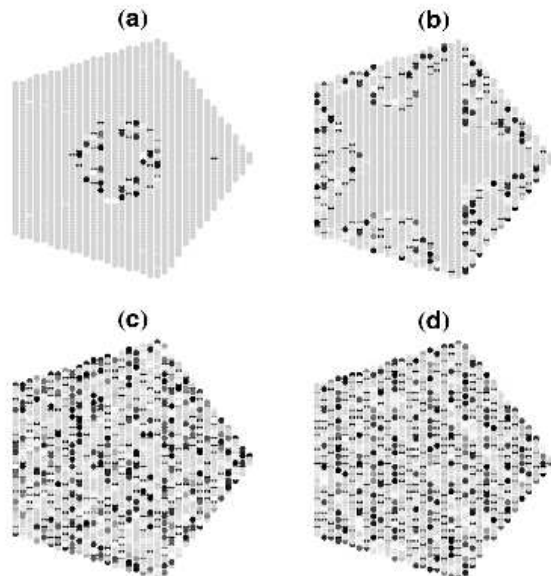


FIG. 8: Intensity plots in perpendicular space representing the probability $\psi_i(E)^2$ for different energies E (a darker shade corresponds to a higher probability): a) $E = 6.469$ b) $E = 3.0000$ c) $E = 0.8887$ d) $E = 0.1692$

ratio decreases as $1/N$ for truly extended states, tends to a constant for localized states, and has an intermediate behavior scaling as $N^{-\beta}$ for the so-called critical states. This quantity has been much studied in the case of tight-binding models for electrons in disordered systems, in particular, close to or at the critical disorder for the metal-insulator transition (MIT)²². For electrons in the Penrose and Ammann-Kramer-Neri tilings, Grimm et al²³ have found a distribution of values of β ranging between 0.5 and 1. Turning now to our spin problem, Fig.9 shows the results for $\log(P^{-1}(E))$ versus E for the Taylor approximants for three different sizes. (Note: the values have been calculated separately for each sublattice, according to the corresponding sector Ω^\pm of the eigenvalue spectrum). The fluctuations in the IPR tend to be quite large from one energy to the next, (note that the figure is plotted on the logarithmic scale), however, the smoothed IPR is an increasing function of E over most of the energy spectrum. There is a noticeable dip in some of the IPR values as the energy approaches the value $E \approx 3$, and at $E = 3$ the value of the IPR does not reflect the spatial extent of the eigenstates, because of the mixing of the macroscopically degenerate states at this energy.

Fig.9 shows the most marked size dependence in the region of small energies, in accord with our earlier observation that states relatively delocalized at low energy. At high energies, the states are more localized, and the size dependence is accordingly smaller.

As a general remark, results for the IPR should be treated with precaution, in the case of quasiperiodic systems, as compared with disordered ones. In the latter

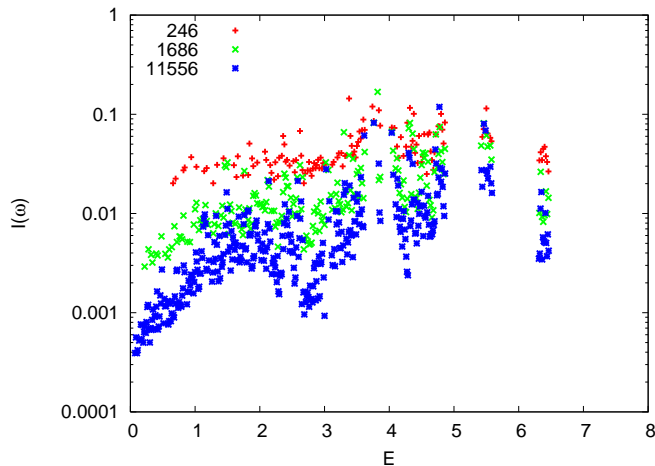


FIG. 9: Inverse participation ratio (IPR) plotted on a log scale as a function of the energy for three successive Taylor approximants

case, away from the MIT, the decay of the wavefunctions is typically exponential, and degenerate states are unlikely. In the quasicrystal, exactly degenerate states do occur at special values of the energy ($E = 3$ here), which leads to an IPR value equal to that of extended states, due to linear combinations of localized states. Our results for the IPR, taken together with the preceding analyses of the wavefunctions, indicate that wavefunctions can be considered to be two dimensional, and power law extended in the lower end of the spectrum. The average value of β , found by fitting the form $P^{-1}(E) \propto N^{-\beta}$ found in this region is $\beta \approx 0.9 \pm 0.1$.

The multifractal character of wavefunctions for quasiperiodic Hamiltonians can be considered to be established in a number of one dimensional models²⁶ and strongly indicated in a number of two dimensional systems including the tight-binding model for electrons²³ and the phonon problem²⁷, and even in three dimensional models²⁸. The scaling properties of the wavefunctions can be investigated by calculating the $f(\alpha)$ spectrum. As $f(\alpha)$ depends on system size, and our system sizes are rather small, an extrapolation to infinite size is not without risk. Nevertheless, we have investigated the multifractal scaling properties in the low energy end of the spectrum, where the states are extended, and have a patchy structure, with peaks and valleys spaced farther and farther apart as energy decreases – see Figs. 7c) and d). We find evidence for a nontrivial distribution of exponents in the limit of large system sizes. Fig.10 shows the results of a multifractal analysis of two representative low energy states for three system sizes. The shape is a priori size dependent, and state dependent as well. One can nevertheless distinguish a smooth functional form of the $f(\alpha)$ function in each case. The curves have a maximum at $\alpha(0) \sim 4$ with $f[\alpha(0)] = 2.0$, which is the dimension of the support – also called similarity

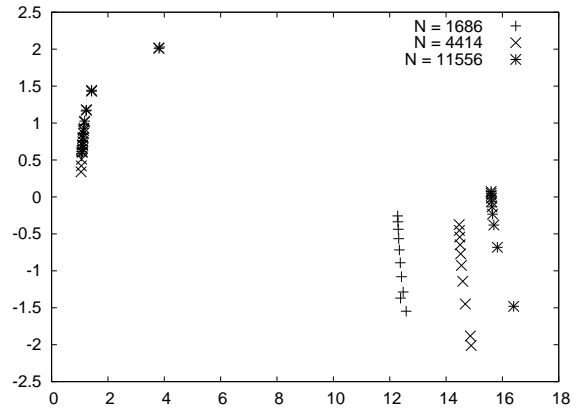


FIG. 10: Some examples of $f(\alpha)$ plots for small energy eigenstates in three Taylor approximants.

dimension – of the wavefunction of this system. The so-called information dimension for these wavefunctions is given by $f[\alpha(1)] = \alpha_1$ (also known as D_1). It corresponds to the intersection of the $f(\alpha)$ curve and a straight line of slope 1 and we find $\alpha_1 \approx 1.5$. For comparison, for a three dimensional system at the metal-insulator transition (MIT) the critical values have been found to be²⁹ $\alpha(0) = 4$ and $\alpha(1) = 2$.

V. RESULTS FOR GROUND STATE ENERGY AND STAGGERED MAGNETIZATIONS

A. Ground state energy

The ground state energy per site is found from Eq.5 for the periodic approximants of size N ranging from 96 to 11556. The energies are shown plotted against $N^{-3/2}$ in the figure 11. This is the expected power law for the ground state finite size correction in two dimensional periodic systems. We find that it is obeyed on the average in the Taylor approximants, with deviations that get smaller as size increases. Our extrapolation to infinite size gives an asymptotic value $E_0 = -0.643(0) \pm 0.0001$. The sign of the deviations varies with system size, and we believe this may be due to the defects present in the Taylor approximants. Since each approximant was obtained by a different rational section in five dimensional space, the distribution of local environments differ from sample to sample. In²¹ it was argued that the ground state energy of the tiling may depend in a simple way on moments of the variable zS . The first moment is just the average value of $zS = 4S$ in all cases. However $\langle (zS)^{-1} \rangle$ varies from sample to sample, and this possibly accounts for the sign and magnitude of the observed deviations from the straight line power law behavior.

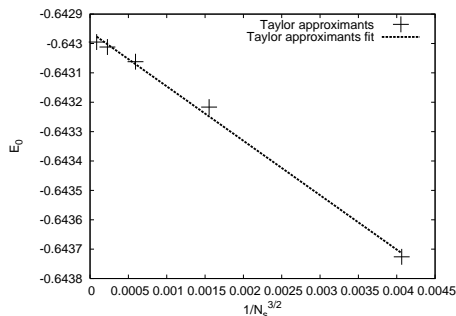


FIG. 11: The scaling of ground state energy of the Taylor approximants with system size

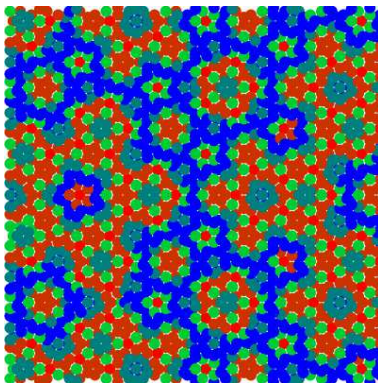


FIG. 12: A portion of a Taylor approximant with vertices colored according to the value of the onsite magnetization (magnetization values : red (small), green (intermediate) blue (highest))

B. Staggered local magnetizations

The absolute value of the local magnetizations in the ground state are given in linear spin wave theory by

$$m_s(i) = |\langle S_i^z \rangle| = S - \sum_{k > \frac{N}{2} - 1} |A_{ik}|^2 \quad (i \leq N/2)$$

$$m_s(j) = |\langle S_j^z \rangle| = S - \sum_{k \leq \frac{N}{2} - 1} |B_{jk}|^2 \quad (j > N/2) \quad (12)$$

Fig.12 represents how local magnetizations vary in space on a portion of the Penrose tiling. The color of the circles around each vertex varies from red (small magnetization) to blue (high magnetization). The lowest values of staggered magnetization are found on a certain subset of $z = 5$ sites, as will be discussed further below. The largest values are found on the low coordination sites of $z = 3$.

Fig.13 indicates how values of the local magnetizations vary with z value for system size $N = 4414$. The figure shows the average values and the standard deviations of $m_i(z)$ for each value of z , as obtained in LSW theory and from QMC, as reported in¹¹. Finite Penrose sam-

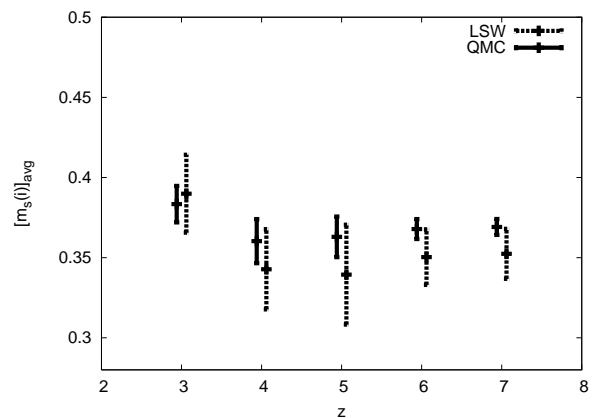


FIG. 13: Averages and standard deviations of the local staggered magnetization as a function of z for $N=4414$ (LSW theory (dashed line) QMC (continuous line))

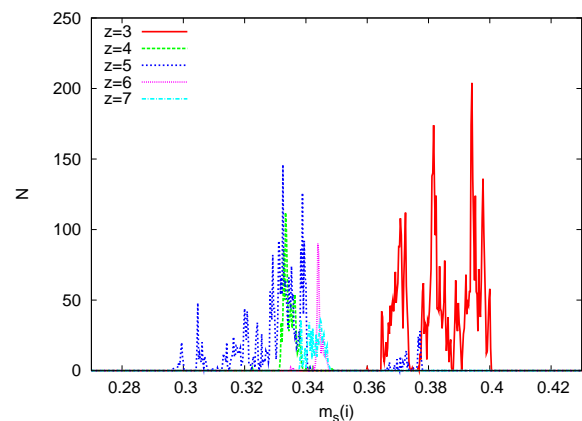


FIG. 14: Probability distribution of the local staggered magnetizations for the five different values of z ($N=11556$)

ples gave the same results as the periodic approximants when the sites on the free boundary layer were excluded from the analysis. The figure shows that Quantum Monte Carlo gives a narrower spread of the magnetization. Linear spin wave theory clearly overestimates the fluctuations from average behavior, giving a too high value for $Z = 3$ and too low values for higher values of z . We show as an example, the details of the distribution of values obtained for $z = 3$ in Fig.14. There is a continuum of values, as expected for a quasiperiodic structure, but also some pronounced peaks, corresponding to specific local configurations. We explain these features in terms of the next nearest neighbor configurations present on the tiling, as seen in the next section. The five-fold sites come also in three main categories, as shown in Table 1, and this will be taken up in more detail further below.

The size dependence of the magnetizations can be seen in Fig.15, where we show the values of the staggered magnetization in six different sample sizes ($N = 96$ to

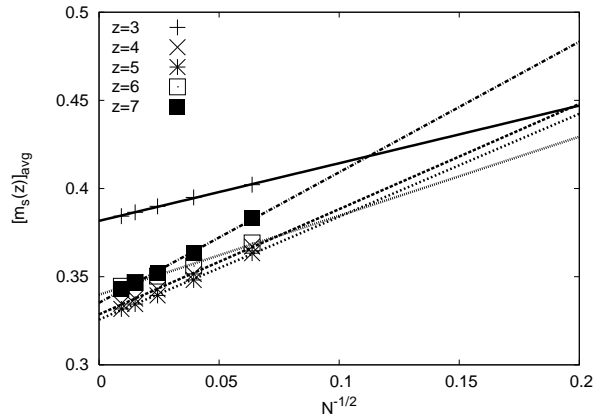


FIG. 15: System size dependence of the average local staggered magnetization for each coordination number z (lines indicate fit to power law $N^{-1/2}$)

$N = 11556$). We show the scaling of the average value of m_i for a given z calculated for each of the six approximants in Fig.15. The averages are seen to obey a scaling with $N^{-1/2}$ as in periodic systems.

We now turn to the explanation of the fluctuations observed in Fig.13 of the average staggered magnetization with z . This behavior can be explained with the help of a simple star cluster model, discussed in Sec.VI.

C. Perpendicular space representation of the ground state staggered magnetization

We show, in Fig.16, two sets of projections onto perpendicular space of the vertices of the Taylor approximants. The corresponding onsite magnetizations, as calculated for the tiling in real physical space, are colored according to their values as previously, in Fig.12. The figures show that, as expected, the domain corresponding to each coordination number has a distinct color. The colors are not absolutely uniform since no two sites are identical. Self-similar patterns can be investigated using this type of representation, however our system sizes are not large enough to enable a quantitative analysis of self-similarity in the ground state. Fig.16a shows the domain corresponding to the F sites, as a central star-shaped region, which has the lowest m_{si} values. The S sites project into a different star-shaped domain shown in Fig. 16b, and can be seen to have a bigger value of the staggered local magnetization. We mentioned that the Penrose tiling is invariant under the inflation transformation where edge lengths are expanded by a factor τ . If there is any self similarity of the ground state under an inflation operation, it can be perceived on the perpendicular space magnetization map as pairs of similar patterns in regions which are related via an inflation transformation.

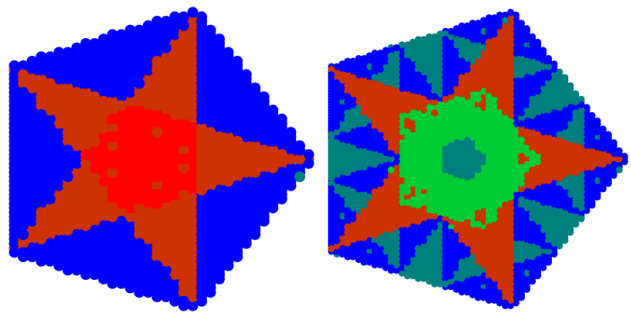


FIG. 16: (Color online) Fig.12 represented in perpendicular space. Two planes are shown (corresponding to $z_{\perp} = 1, 2$) (magnetization values : red (small), green (intermediate) blue (highest))

VI. PREDICTIONS USING THE HEISENBERG STAR MODEL.

We first consider the effects of variation of the number of nearest neighbors using a simple Heisenberg star model, as first outlined in¹⁶. A central spin \mathbf{S}_0 is coupled to z neighbors \mathbf{S}_j . The Hamiltonian $H = \sum_{j=1}^z \mathbf{J}\mathbf{S}_0 \cdot \mathbf{S}_j$, can be expanded in boson operators a (describing the center site spin fluctuations) and b_j , as described in¹⁶. The corresponding magnetizations are respectively $m_0 = S - \delta m_0$ and $m_j = S - \delta m_j$ where (for $z > 1$)

$$\begin{aligned} \delta m_0 &= 1/(z-1) \\ \delta m_j &= 1/z(z-1) \end{aligned} \quad (13)$$

Quantum fluctuations of the center spin are thus larger than those of the outer spins. This is a consequence of the fact that in such clusters, the classical term, which creates an onsite potential $V_0 \propto z$, thereby discouraging boson formation on the center site, is dominated by the transverse terms. These terms in $a^\dagger b_j^\dagger$ create and annihilate boson pairs on each link, leading to quantum fluctuations being greater for sites with more neighbors.

This cluster model is a first approximation. In order to explain the multiple peaks in the values of m_{si} seen numerically for a given z , we must take into account longer range structural details.

We consider therefore the two tier Heisenberg star shown in Fig.17, as described in¹¹. The Hamiltonian of this cluster is linearized after introducing Holstein-Primakoff operators a_0, a_i , ($i = 1, \dots, z'$) and b_j , ($j = 1, \dots, z$) The resulting expression for the center site magnetization is

$$m_s(z, z') = \frac{1}{2} - \frac{z f_1^2(z, z')}{f_2^2(z, z') - z f_1^2(z, z') - 4z'}, \quad (14)$$

where $f_{1(2)} = -z' \pm (2 - z + \sqrt{4 - 4z + (z + z')^2})$.

The main new feature of $m_s(z, z')$ is its non-monotonicity. m is shown plotted against z for various

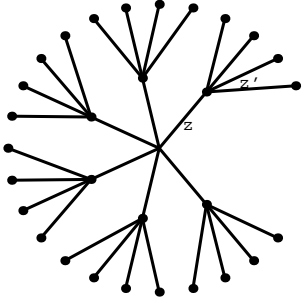


FIG. 17: Two-tier Heisenberg star

values of z' in Fig.18. For each of the curves of fixed z' , a shallow minimum is seen to occur for values $z \sim 1 + z'$, that is, when the coordination numbers of the center site and the nearest neighbors are matched.

Returning to the Penrose tiling and approximants thereof, we use the number of next nearest neighbor bonds $n(z)$ to classify sites of a given z . The $z = 3$ sites can be classified in three subgroups, depending on z' , as shown in Table 1. Fig.14 shows the values of $m_s(z, z')$ obtained for the Penrose tiling sites. To take the case of $z = 3$, three values corresponding to three main local configurations are found, to be compared with the three principal peaks of the red curve in Fig.14. The substructures arise due to differences in the third nearest and further neighbor configurations.

The number of next nearest neighbors also serves to distinguish between the different $z = 5$ sites, of which there are three main types. There are two varieties of five-fold symmetric sites: the football-shaped clusters (F) and the star-shaped clusters (S). The former have $z' = 2$, while the latter have $z' = 4$. The F sites thus have the smallest onsite magnetizations and the S-sites, on the contrary, have the largest onsite magnetization. The remaining (most frequently occurring) $z = 5$ sites which do not have a local five-fold symmetry have intermediate values of z' .

z	z' (corresponding frequency)	$m_s(z, z')$
3	4 (31%), 4.33 (27%), 4.67 (42%)	0.41, 0.42, 0.43
4	3 (100%)	0.36
5	2 (14%), 2.4 - 3.2 (81%), 4 (5%)	0.26, 0.35, 0.41
6	3 (100%)	0.37
7	2.3 (100%)	0.33

Table 1. Values of z' (and their frequencies) for each coordination z and the predicted values of $m(z, z')$ using Eq.14

A. Fourier transformation

Fourier transforms of the original structure, as well as that of the antiferromagnetic ground states are shown in

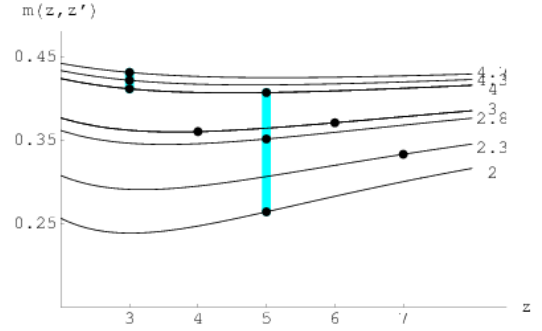


FIG. 18: $m_s(z, z')$ plotted as a function of z (see text) for selected values of z' (as given in Table 1).

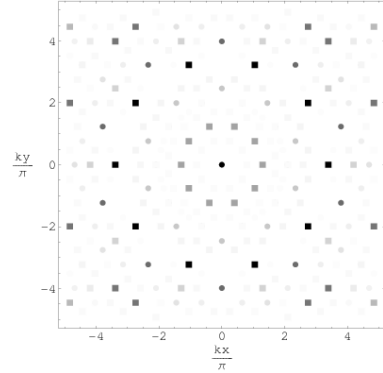


FIG. 19: Intensity plot of the static longitudinal magnetic structure factor $S^{\parallel}(\mathbf{k})$ for the $N = 4414$ Taylor approximant. The highest intensity peaks are shown in the figure at positions that are indicated by circles(squares) for the magnetic (nonmagnetic) structures respectively. The relative intensity is denoted by a linear gray scale ranging between zero (white) and maximum intensity (black).

19. The highest intensity peaks are shown in the figure at positions that are indicated by circles(squares) for the magnetic (nonmagnetic) structures respectively. Peaks can be indexed using four indices which are integers for non-magnetic peaks and integer or half-integer for the magnetic peaks. As in the case of the octagonal tiling⁶ the half integer indices arise due to the doubling in size of the antiferromagnetic unit cell in five dimensions. This, coupled with the extinctions in the structure factor rule due to the multiplicity of each unit cell, then leads³⁰ to the observed “shifting” or “displacement” of the magnetic peaks with respect to the nonmagnetic ones.

VII. CONCLUSIONS

We have presented a detailed analysis of energies and wavefunctions of magnon eigenmodes found by numerical diagonalization of the Heisenberg model on approximants of the Penrose tiling in the linearized spin wave

approximation. A linear dispersion is found at low energies, as in other bipartite antiferromagnets, despite the lack of translational invariance. This is to be expected in the long wavelength limit, where structural details do not play a role, as known in related studies of low energy vibrational modes in quasicrystals or in glasses. The effective spin wave velocity as obtained from the low energy spectrum was found and compared with that in the square lattice and the octagonal tiling.

The spatial dependence of eigenmodes has been investigated. It is shown that in different ranges of energies, states have their support on sites of a different given coordination number. At low energies, in contrast, all sites participate, and the resulting eigenstates are relatively extended, as seen by the absolute values and the size dependence of the participation ratio. A few low energy extended eigenstates are analysed for their multifractal scaling properties, including the similarity dimension and information dimensions. In general, our studies indicate that the dimensionality of the states diminishes progressively as energy increases.

We find the ground state energy of this antiferromagnet, and give the distribution of the local magnetizations as a function of site coordination number. Perpendicular space projections are shown to demonstrate the simplicity of the ground state in this representation. The structure factor of the magnetic state is found and compared with that of the nonmagnetic state.

A simple analytical model, the two-tier Heisenberg star, is presented to explain our results. The role of next neighbors is shown to be nontrivial, and explains the z dependence of the onsite staggered magnetizations.

Acknowledgments

We would like to thank M. Duneau and S. Wessel for many useful discussions. A.Sz. was supported by the European Commission, through a Marie Curie Foundation contract, MEST CT 2004-51-4307, during the course of this work.

APPENDIX A: OBTAINING THE PENROSE TILING AND ITS APPROXIMANTS BY PROJECTION

1. The perfect Penrose tiling.

The perfect Penrose tiling can be obtained by the projection onto the xy plane of selected vertices of a five dimensional (5D) cubic lattice. A vertex, designated by the five-dimensional vector n_1, n_2, \dots, n_5 , is selected for projection if its projection in the three dimensional “perpendicular space” belongs in the region W (called the “selection window”). The projection matrices M_{\parallel} and M_{\perp} give the real space coordinates $x_{\parallel}, y_{\parallel}$ and perpendicular space coordinates $x_{\perp}, y_{\perp}, z_{\perp}$ respectively are

$$M_{\parallel} = \sqrt{\frac{2}{5}} \begin{pmatrix} 1 & \cos \theta & \cos 2\theta & \cos 2\theta & \cos \theta \\ 0 & \sin \theta & \sin 2\theta & -\sin 2\theta & -\sin \theta \end{pmatrix} \quad (\text{A1})$$

$$M_{\perp} = \sqrt{\frac{2}{5}} \begin{pmatrix} 1 & \cos 2\theta & \cos \theta & \cos \theta & \cos \theta \\ 0 & \sin 2\theta & -\sin \theta & \sin \theta & -\sin 2\theta \\ \frac{1}{\sqrt{2}} & \frac{1}{\sqrt{2}} & \frac{1}{\sqrt{2}} & \frac{1}{\sqrt{2}} & \frac{1}{\sqrt{2}} \end{pmatrix} \quad (\text{A2})$$

where $\theta = 2\pi/5$.

For a vertex to be selected, its perpendicular coordinates must fall within the rhombic icosahedron W which is the projection of the 5D unit cube. In view of the expression for M_{\perp} given above, W decomposes into four subdomains W_i , corresponding to $z_{\perp} = 1, 2, 3$, or $4 \pmod{5}$. The acceptance window W_i in each of these four planes in the perpendicular space is a pentagon. Two such pentagons are shown in Fig.20 (corresponding to $z_{\perp} = 1$ and 2), the other two being the same upto an inversion.

The parity of the vertex as given by $\sum n_i$ determines the sublattice to which it belongs. Thus, the points that project into the planes $z_{\perp} = 1, 3$ correspond, say, to sublattice A, while the planes $z_{\perp} = 2, 4$ correspond to sublattice B. In the infinite tiling, the two sublattices are equivalent, and the “even” and “odd” windows are the same upto an inversion.

Finite samples of arbitrarily large size can be readily generated using this selection criterion, by considering large enough volumes of the 5D cubic lattices.

Turning to the question of the local environments, we show in Fig.20 a portion of the Penrose tiling, with vertices of different z colored differently. When these vertices are represented in perpendicular space, the colored domains are clearly seen corresponding to each value of z . We have seen that there are three types of $z = 5$ sites, including the F and S subsets. The F sites project onto the central pentagonal regions in the planes $z_{\perp} = 1$ and 4, while the S sites project into the central pentagons in the planes $z_{\perp} = 2$ and 3.

2. The Taylor approximants.

To obtain periodic approximants, the physical plane has to be tilted so that it has a rational orientation (that can be chosen arbitrarily close to the original irrational orientation). There will then be two lattice vectors \vec{A}_1 and \vec{A}_2 of the 5D lattice, whose projections give the periodic lengths in the physical plane. This is achieved in practice by using an oblique projection \tilde{M}_{\perp} appropriately defined depending on the choice made for \vec{A}_1 and \vec{A}_2 . The resulting selection window \tilde{W} will be a deformed rhombic icosahedron. Details of the construction of the projection operators for the so-called Taylor approximant can be found in¹⁸. This method can be used

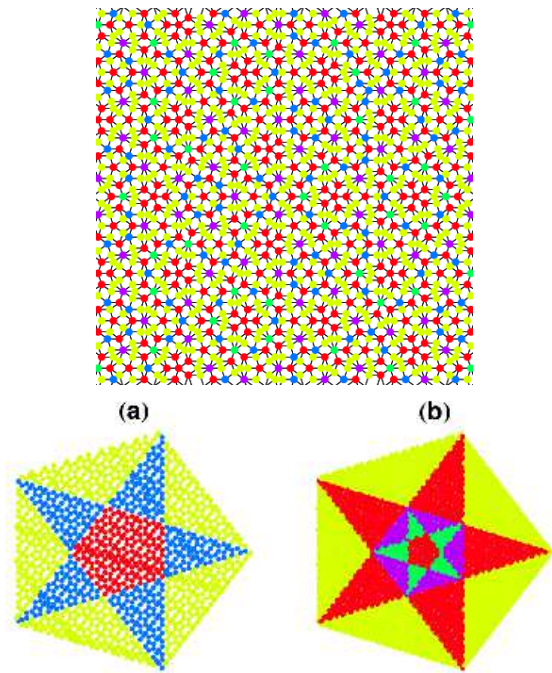


FIG. 20: (Color online) (upper) Portion of the tiling showing vertices colored differently, according to coordination number z (lower) The same tiling after projection into perpendicular space (a) the plane $z_{\perp} = 1$, b) the plane $z_{\perp} = 2$)

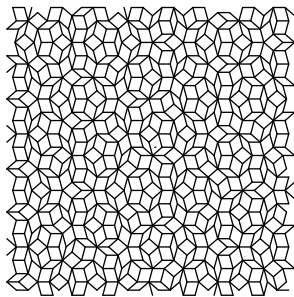


FIG. 21: Taylor τ^3 approximant (N=644 sites)

to obtain bigger systems, and we have considered six approximants, that we labelled Taylor, Taylor τ , ..., upto Taylor τ^6 (containing 11556 sites). (Note: the original Taylor approximant, consisting of 36 sites is too small for use in our analysis). As an example, in the case of our Taylor τ^3 approximant (N=644 sites), we have

$$\vec{A}_1 = \{10, 3, -8, -8, 3\} \quad (\text{A3})$$

$$\vec{A}_2 = \{0, 8, 5, -5, -8\} \quad (\text{A4})$$

with the resulting rectangular shape of sides $L_x = 24.7984$ and $L_y = 21.0948$ (see Fig.21).

Note: In our calculations, we have used systems having sublattices A and B of the same size. This was achieved by shifting the selection windows in perpendicular space, until the number of A and B sublattice points selected are equal.

¹ B. Charrier, B. Ouladdiaf and D. Schmitt, **78** 4637 (1997); S. Kashimoto, S. Matsuo, H. Nakano, T. Shimizu and T. Ishimasa, *Solid State Commun.* **109** 63 (1999); T.J. Sato, H. Takakura, A. P. Tsai, K. Shibata, K. Ohoyama, and K. H. Andersen, *Phys. Rev. B* **61** 476 (2000);
² T.J. Sato, H. Takakura, A.P. Tsai and K. Shibata, *Phys. Rev. B* **73** 054417 (2006)
³ E. Y. Vedmedenko, H. P. Oepen, and J. Kirschner, *Phys.Rev.Lett.* **90** 137203 (2003).
⁴ H. Matsuo, A. Aimurula, T. Ishimasa, S. Motomura and H. Nakano, *Philos. Mag.* **86** 741 (2006).
⁵ S. Wessel, A. Jagannathan and S. Haas, *Phys. Rev. Lett.* **90**, 177205 (2003).
⁶ S. Wessel and I. Milat, *Phys. Rev. B* **71**, 104427 (2005).

⁷ A. Jagannathan, *Phys. Rev. Lett.* **92** 047202 (2004).
⁸ A. Jagannathan, *Phys. Rev. B* **71** 115101 (2005)
⁹ R. Penrose, *The Math. Intelligencer* **2**, 32 (1979).
¹⁰ P. J. Steinhardt and S. Ostlund in *The Physics of Quasicrystals*, World Scientific, Singapore 1987.
¹¹ A. Jagannathan, A. Szallas, S. Wessel and M. Duneau, *Phys. Rev. B* **75** 212407 (2007)
¹² E. Manousakis, *Rev. Mod. Phys.* **63**,1 (1991).
¹³ Zheng Weihong and C. J. Hamer, *Phys. Rev. B* **47** 7961 (1993); A. W. Sandvik, *Phys. Rev. B* **56** 11678 (1997); H. J. Schulz, T.A.L. Ziman and D. Poilblanc, *J. Phys. I (France)* **6** 675 (1996); R. F. Bishop, D. J. J. Farnell, S.E. Krueger, J. B. Parkinson, J. Richter and C. Zeng, *J. Phys. Cond. Mat.* **12** 6887 (2000)

- ¹⁴ J. Richter, J. Schülenburg and A. Honecker, in *Quantum Magnetism in Two Dimensions: From Semiclassical Néel Order to Magnetic Disorder*, Lecture Notes in Physics, Vol. 645 (Springer-Verlag Berlin Heidelberg, 2004) p. 85
- ¹⁵ J. D. Reger, J. A. Riera and A. P. Young, *J. Phys.: Condens. Matt.* **1** 1855 (1989)
- ¹⁶ A. Jagannathan, R. Moessner and S. Wessel, *Phys. Rev. B* **74** 184410 (2006)
- ¹⁷ M. D. Mermin and H. Wagner, *Phys. Rev. Lett.* **17** 1133 (1966); P.C. Hohenberg, *Phys. Rev.* **158** 383 (1967)
- ¹⁸ M. Duneau and M. Audier in *Lectures on Quasicrystals, Winter School Aussois, January 1994*, edited by F. Hippert and D. Gratias (Les Editions de Physique, Les Ulis, 1994).
- ¹⁹ R. M. White, M. Sparks and I. Ortenburger, *Phys. Rev.* **139**, A450 (1965).
- ²⁰ E. Anderson, Z. Bai, C. Bischof, S. Blackford, J. Demmel, J. Dongarra, J. Du Croz, A. Greenbaum, S. Hammarling, A. McKenney, and D. Sorensen, *LAPACK Users' Guide*, 3rd ed. (Society for Industrial and Applied Mathematics, Philadelphia, 1999)
- ²¹ A. Jagannathan, *Phys. Rev. Lett.* **94** 029702 (2005)
- ²² B. Kramer and A. MacKinnon, *Rep. Prog. Phys.* **56** 1469 (1993)
- ²³ U. Grimm and M. Schreiber in *Quasicrystals - Structure and Physical Properties*, ed. H.-R. Trebin (Wiley-VCH, Weinheim, 2003)
- ²⁴ M. Quilichini and T. Janssen, *Rev. Mod. Phys.* **69** 277 (1997)
- ²⁵ T. Fujiwara, M. Kohmoto and T. Tokihiro, *Phys. Rev. B* **40** 7413 (1989)
- ²⁶ T. Janssen and M. Kohmoto, *Phys. Rev. B* **38** 5811 (1988)
- ²⁷ J. Los, T. Janssen and F. Gähler, *Int. J. Mod. Phys. B* **7** 1505 (1993)
- ²⁸ J. Los, T. Janssen and F. Gähler, *J. Phys. I (Fr.)* **3** 107 (1993)
- ²⁹ H. Grussbach and M. Schreiber, *Phys. Rev. B* **51** 663 (1995)
- ³⁰ Ron Lifshitz, *Mat. Sci. Engg* bf 294 508 (2000)